ISSN 2791-0091 (print); 2790-8119 (online) https://doi.org/10.26599/NRE.2023.9120055

Binder-free Li-O₂ battery cathodes using Ni- and PtRu-coated vertically aligned carbon nanofibers as electrocatalysts for enhanced stability

Syed Shoaib Hassan Zaidi¹, Sabari Rajendran², Archana Sekar², Ayyappan Elangovan², Jun Li², and Xianglin Li^{1,3} (🖂)

- ¹ Department of Mechanical Engineering, University of Kansas, Lawrence, KS 66045, USA
- ² Department of Chemistry, Kansas State University, Manhattan, KS 66506, USA
- ³ Department of Mechanical Engineering and Materials Science, Washington University in St. Louis, St. Louis, MO 63130, USA

Received: 29 January 2023 / Revised: 10 February 2023 / Accepted: 11 February 2023

ABSTRACT

The development of an ideal cathode for Li-O₂ battery (LOB) has been a great challenge in achieving high discharge capacity, enhanced stability, and longevity. The formation of undesired and irreversible discharge products on the surface of current cathode materials limit the life span of the LOB. In this study, we report the systematic electrochemical study to compare the performance of LOB employing a unique graphitic nanostructured carbon architecture, i.e., vertically aligned carbon nanofiber (VACNF) arrays, as the cathode materials. Transition metal (Ni) and noble metal alloy (PtRu) are further deposited on the VACNF array as electrocatalysts to improve the discharge/charge processes at the cathode. The structure of as-prepared electrodes was examined with the field emission scanning electron microscopy, high-resolution transmission electron microscopy, and X-ray photoelectron spectroscopy (XPS). The LOB with VACNF-Ni electrode delivered the highest specific and areal discharge capacities (14.92 Ah·g⁻¹, 4.32 mAh·cm⁻²) at 0.1 mA·cm⁻² current density as compared with VACNF-PtRu (9.07 Ah·g⁻¹, 2.62 mAh·cm⁻²), bare VACNF (5.55 Ah·g⁻¹, 1.60 mAh·cm⁻²) and commercial Vulcan XC (3.83 Ah·g⁻¹, 1.91 mAh·cm⁻²). Cycling stability tests revealed the superior performance of VACNF-PtRu with 27 cycles as compared with VACNF-Ni (13 cycles), VACNF (8 cycles), and Vulcan XC (3 cycles). The superior cycling stability of VACNF-PtRu can be attributed to its ability to suppress the formation of Li₂CO₃ during the discharge cycle, as elucidated by XPS analysis of discharged samples. We also investigated the impact of carbon cloth and carbon fiber as cathode electrode substrate on the performance of LOB.

KEYWORDS

lithium oxygen battery, vertically aligned carbon nanofibers, Ni, PtRu, cathodes, stability

1 Introduction

In order to curb the detrimental impact of climate change, the world is shifting from fossil fuels towards renewable energy sources. Li-ion battery has brought a revolution in electronic devices. Nonetheless, its intrinsic low energy density (250 Wh·kg⁻¹) is inadequate to meet high energy demands, especially in electric vehicles (EVs). Consequently, it is imperative to develop alternative energy storage systems. Lithium-oxygen batteries (LOBs) have been considered an attractive alternative as a nextgeneration battery that has the ability to supersede current rechargeable batteries [1]. Despite having a tremendously high theoretical energy density of $\sim 3500~{\rm Wh·kg^{-1}}$ (by mass of Li₂O₂), the practically achievable energy density is estimated between 500–900 Wh·kg⁻¹, which is far from commercial application till date [2–7]. Low cycling stability, poor round-trip efficiency, low-

rate capability, and limited mass transfer of oxygen and Li ions are some of the bottleneck challenges that stymied its progress.

Contrary to Li-ion or Na-ion battery which involves the storage of active material inside the battery, metal-air battery possesses the unique feature of an open system. The active material (oxygen) is supplied from the outside to the porous cathode instead of being stored inside the battery housing. Consequently, the gravimetric energy density may be theoretically increased by many folds as compared with Li-ion batteries. An aprotic, nonaqueous LOB comprises a Li chip anode, an electrolyte-soaked separator, and a porous cathode.

The mechanism of discharge/charge cycles of LOB is presented in Eqs. (1)–(3) [8]. During the discharge cycle, the reaction begins at the anode where Li metal is oxidized to Li⁺ ions (Eq. (1)). These Li⁺ ions are transported through the electrolyte to the porous

© The Author(s) 2023. Published by Tsinghua University Press. The articles published in this open access journal are distributed under the terms of the Creative Commons Attribution 4.0 International License (http://creativecommons.org/licenses/by/4.0/), which permits use, distribution and reproduction in any medium, provided the original work is properly cited.

Address correspondence to lxianglin@wustl.edu



cathode where they react with the incoming oxygen/air to form Li_2O_2 . This reaction is called oxygen reduction reaction (ORR), shown in Eq. (2). The Li_2O_2 generated during the discharge cycle accumulates on the cathode surface [9]. During the charge cycle, the deposited Li_2O_2 decomposes to liberate O_2 and Li^+ ions. This process is called oxygen evolution reaction (OER), shown in Eq. (2). The overall reaction is shown in Eq. (3)

Anode:
$$2Li \rightleftharpoons 2Li^+ + 2e^-$$
 (1)

Cathode:
$$2Li^+ + 2e^- + O_2 \rightleftharpoons Li_2O_2$$
 (2)

Overall:
$$2\text{Li} + \text{O}_2 \rightleftharpoons \text{Li}_2\text{O}_2(E_{\text{cell}}^{\circ} = 2.96 \text{ V})$$
 (3)

The formation of Li₂O₂ as a result of ORR passivates the cathode surface owing to its insulating properties and physically clogs pores due to insolubility in nonaqueous electrolytes. Consequently, high mass transfer resistance leads to limited capacity during the discharge cycle [10-13]. Ideally, Li₂O₂ should disintegrate completely during the charge cycle but the instability of the carbon cathode and electrolyte results in undesired side reactions. This leads to the deposition of irreversible discharge products e.g., Li₂CO₃ on the cathode surface, thereby decreasing the surface area for Li₂O₂ and increasing ohmic resistance. These factors contribute to gradual capacity fading and eventually death of battery [14]. Since the bandgap of Li₂CO₃ is wider than Li₂O₂, this requires high electrical energy to oxidize it completely, and consequently, the charge potential surpasses 4.0 V in subsequent cycles. This further deteriorates the battery life as this surge in charge voltage leads to electrolyte decomposition. An ideal cathode should have a high surface area (for maximum reaction sites), high porosity (for maximum mass transfer), high electronic conductivity (for reduced resistance), and high stability that enables it to survive in the corrosive environment of battery [15, 16]. Owing to the high electrical conductivity, low cost, and lightness, various forms of carbon, including mesoporous carbons [17], graphene [18], carbon nanotubes (CNT) [19], and carbon nanofibers (CNF) [20-23] have been incorporated in cathodes. Although carbonaceous materials are preferred as a cathode material owing to their numerous advantages, nonetheless, irreversible side reactions arising from its instability in the presence of discharge products, polymer binder and electrolytes during OER are detrimental for the longevity of the battery. Additionally, sluggish kinetics in the formation and oxidation of Li₂O₂ leads to low round-trip efficiency, poor rate capability and shorter cycle life [7, 24]. Consequently, these cathodes have often been modified with catalysts, including metal nanoparticles [25], metal oxides [26, 27], heteroatom doping [28], etc. The prime function of catalysts is to improve ORR and OER kinetics by reducing the activation barrier of reacting species. This results in a reduction in cell polarization, higher rate capability, mitigation in parasitic reactions due to instability of carbon (especially at higher voltage) and improved cycling stability [29].

Ko et al. reported the performance of various combinations of noble metal alloys, including Pt-Ru, Pd-Ir, and Pt-Pd supported on Vulcan XC and showed that Pt-Ru/C exhibited highest discharge capacity (346 mAh·g⁻¹) followed by Pt-Pd (153 mAh·g⁻¹) and Pd-Ir (135 mAh·g⁻¹) at a current density of 0.2 mA·cm⁻² [30]. Wu et al. compared the LOB performance by employing pure Pt and Pt-Ru catalysts supported on Vulcan XC. They demonstrated that Pt-Ru achieved highest cycling stability (17 cycles) as compared with pure Pt catalysts (< 5 cycles) at a current density of 100 mA·g⁻¹. Upon discharge product examination, they revealed

that Pt-Ru produced poorly crystalline Li₂O₂ which leads to lower charge overpotential and higher stability [31]. Yang et al. exploited Pt₂Ru/Vulcan XC as a LOB cathode and attained a discharge capacity of 5386 mAh·g⁻¹ in comparison with Vulcan XC (4376 mAh·g⁻¹) at a current density of 0.05 mA·cm⁻². Pt₂Ru/Vulcan XC also maintained lower discharge and charge overpotential compared with pure carbon electrode [32]. Recently, Jung et al. employed LOB cathode with a quaternary combination of noble metal catalysts (Pt-Pd-Au-Ru) and were able to achieve three times higher discharge capacity (9130 mAh·g-1) and reduced charge overpotential (0.45 V) as compared with pristine CNF electrode [25]. Li and coworkers developed a LOB cathode by mixing Fe₃O₄@C and PtRu nanoparticles and achieved 7996 mAh·g⁻¹ (vs. 4000 mAh·g⁻¹ with Ketjenblack (KB))at a current density of 200 mA·g⁻¹. The battery was able to cycle 21 and 32 times with 500 and 1000 mAh·g⁻¹ limited capacity, respectively [33]. Jiaqiang et al. utilized binder-free Ni-Co/CNF electrodes and achieved a decent discharge capacity of 8635 mAh·g-1 (vs. 968 mAh·g⁻¹ with CNF) and 60 cycles with 1000 mAh·g⁻¹ cutoff capacity at a current density of 200 mA·g⁻¹ [34].

The above-mentioned studies have exploited either noble metals or transition metal alloys as LOB cathode catalysts. To the best of our knowledge, no previous reports were found with LOB cathode electrodes based on vertically aligned CNF (VACNF) arrays, a unique brush-like vertically aligned three-dimensional CNF architecture with conical graphitic stack internal structure [35, 36], which are further coated with Ni or PtRu films. Ni foam has been widely utilized as a non-carbon based substrate in battery research [37, 38]. However, very few studies incorporated Ni nanoparticles as an electrocatalyst. Zhu and coworkers incorporated Ni/graphene foam in LOB and achieved high discharge capacity (22,035 mAh·g⁻¹) and decent cycling stability (22 cycles) at the current density of 100 mA·g⁻¹ [39]. This indicates that Ni as an electrocatalyst in LOB has a great potential to deliver much higher discharge capacity than expensive noble metals, hence requiring more attention. Conversely, PtRu has been extensively exploited as a noble metal alloy catalyst and proved effective in extending the battery cycle life. In LOBs, however, it has mostly been coupled with commercial carbon as a cathode material, consequently delivering limited performance. Herein, we report the comparison of the electrochemical performance of LOB employed with Ni and PtRu-coated VACNF array cathode, respectively. Binder-free VACNF electrodes were synthesized by direct growth of CNFs on gas diffusion layer (GDL) substrates using a plasma-enhanced chemical vapor deposition (PECVD) technique. VACNF array electrodes were sputtered with a thin film of Ni and PtRu, respectively, at a nominal thickness of 20 nm. The as-prepared electrodes were examined under the field emission scanning electron microscopy (FESEM), high resolution transmission electron microscopy (HRTEM), and X-ray photoelectron spectroscopy (XPS). LOB with VACNF-Ni electrode achieved the highest specific and areal discharge capacity (14.92 Ah·g⁻¹, 4.32 mAh·cm⁻²) among all electrodes. Cycling stability tests suggested the superior performance of VACNF-PtRu with 27 cycles. The deep-discharged electrodes were analyzed under FESEM and XPS to demonstrate the morphology of the discharge product. We also report the impact of the most ubiquitously used carbon GDL substrates, i.e., carbon cloth (CC) and carbon paper (CP), on the battery performance. Several studies have been conducted on the effects of these substrates in fuel cells [40] and flow batteries [41, 42]. But to the best of our knowledge, no such study has been reported for LOBs.

2 Experimental

2.1 Vulcan XC 72R-30% polytetrafluoroethylene (PTFE) electrode preparation

Vulcan XC 72R purchased from Fuel Cell Store was used for coating the GDL substrate 1071 HCB plain CC and Sigracet 29AA CP. Vulcan XC was mixed with PTFE binder (70 wt.%:30 wt.% ratio) in isopropyl alcohol (IPA) and water solution (70 vol.%: 30 vol.% ratio). The mixture was sonicated in Branson bath sonicator for 3–4 h to get all components well combined. The prepared slurry was blade coated on both substrates. The coated substrates were dried for 24 h at room temperature (20 °C) followed by the heat treatment in SentroTech oven at 350 °C under atmospheric conditions for 30 min. The mass loading measured for the electrode of area 0.712 cm² (3/8 diameter) was $0.5\pm0.1~{\rm mg\cdot cm^{-2}}.$

2.2 VACNF-based electrodes preparation

VACNF arrays were grown on Sigracet 29AA CP (for VACNF-Ni only) and 1071 HCB plain CC by PECVD in an Aixtron Black Magic system. The bare substrate was first sputtered with a 22 nm thick Ni film which was converted into randomly distributed Ni nanoparticles by thermal dewetting at 500 °C in the presence of ammonia (NH₃). It was then subjected to 63 sccm of acetylene (C₂H₂) and 250 sccm ammonia (NH₃) in the PECVD process at 750 °C. Each Ni nanoparticle catalyze the growth of a CNF in the tip growth mode perpendicularly to the substrate surface. To achieve the desired length of 8 µm of VACNF, the growth time was set at 60 min. The Ni and PtRu were sputtered at a rate of 0.5 Å·s⁻¹ using Ar⁺ ion beam at the beam energy of 8.0 and 7.2 keV, respectively, to deposit a nominal thickness of 20 nm on VACNF. This nominal thickness corresponds to a Ni mass loading of 17.8 μg·cm⁻² and a PtRu mass loading of 34.2 μg·cm⁻² with respect to the geometric surface area of a flat substrate, which are negligible relative to the mass of VACNFs. The overall mass loadings measured for VACNF electrodes based on CC and CP substrates were 0.29 ± 0.02 and 0.14 ± 0.02 mg·cm⁻² respectively Table S1 in the Electronic Supplementary Material (ESM) summarized the mass loading calculations of VACNF based samples.

2.3 Battery assembly

A widely used commercial organic electrolyte solvent, dimethyl sulfoxide (DMSO) was incorporated in this study. Bis(trifluoromethane)sulfonimide (LiTFSI) is used as Li salt to make 1 M concentration solution. All these materials were purchased from Sigma-Aldrich and used as received. The battery was assembled in an argon-filled Mikrouna glovebox with O2 and H₂O concentrations maintained below 0.1 ppm. Four customized electrodes (Vulcan XC, bare VACNF, VACNF-Ni, and VACNF-PtRu) of 9.5 mm in diameter were employed as the battery cathode. A customized titanium battery frame was used [43, 44]. A cathode electrode was placed on the base of the frame with oxygen channels and a Whatman glass fiber separator (GF/C, 1822-021) with a diameter of 1.58 cm was laid on top of the cathode. The separator was soaked with 90 µL of electrolyte. Finally, a Li chip (0.25 mm thick) with a size of 1.27 cm² was placed on top of the separator, which acts as the anode. The battery was screwed and ready for testing.

2.4 Electrochemical testing

The assembled battery was supplied with pure O_2 (99.99%) supply. In order to remove argon from the electrode assembly, the battery was purged for a minimum of 1 h at the open circuit voltage (OCV). Cyclic voltammetry (CV) tests were conducted using a Biologic SP-150 potentiostat at the scan rate of 0.1 mV·s⁻¹. Galvanostatic discharge/charge capacity tests were performed on a 4-channel Arbin MSTAT4 battery tester. The discharge and charge cutoff voltages used were 2 and 4.5 V, respectively. The cycling stability tests were conducted with a curtailed areal capacity of 0.5 mAh·cm⁻² for all aforementioned electrodes. All tests were conducted at a current density of 0.1 mA·cm⁻² and room temperature (20 °C).

2.5 Material characterizations

Fresh electrodes were analyzed under Topcon/ISI/ABT DS 130F FESEM (Akashi Beam Technology Corporation, Tokyo, Japan). The TEM and scanning TEM (STEM)/energy dispersive spectroscopy (EDS) mapping were imaged using a Tecnai Osiris S/TEM (FEI, Hillsboro, OR) at a 200 kV acceleration voltage. The surface elemental composition of the catalysts was characterized using a PHI 5000 versa XPS system (Chanhassen, MN) with a monochromatized Al K α source (1486.7 eV). Shirley background was used in the curve fitting. The binding energy (BE) of all XPS data was calibrated vs. the standard sp² C 1s peak at 284.60 eV. In order to illustrate the morphology of the discharge products on various cathode electrodes, deep-discharged electrodes were examined by FESEM and XPS.

3 Results and discussions

3.1 Fresh electrodes characterizations

Figure 1 shows the FESEM images of VACNF/CC (Figs. 1(a)-1(c)) and VACNF/CP (Figs. 1(d)-1(f)) at various magnifications. It is evident from Figs. 1(a) and 1(d) that the two substrates exhibit starkly different structures. Carbon fibers in CC constitute a woven structure in comparison with CP which comprises of random arrangement of fibers stacked on top of each other and coated with a carbonaceous film. Figures 1(b), 1(c), 1(e), and 1(f) show the FESEM images of a VACNF array grown on a carbon fiber at the exterior surface of the CC and CP substrate respectively. On average, each VACNF measures 8 μ m in length and 150 nm in diameter with nearest-neighbor distance of $\sim 300-350$ nm.

Figures 2(a)-2(c) show the HRTEM images of a single CNF scraped off from the VACNF array which clearly contains a Ni nanoparticle that catalyzed the CNF growth. The top surface of these Ni nanoparticles is typically covered with a few graphene layers (invisible at this resolution). The sidewall of the CNF is covered with a layer of much smaller Ni nanoparticles (~ 2-5 nm in diameter) which was deposited post CNF growth by ion-beam sputtering, similar to our previous studies [45]. The quantity of the sputtered Ni (and PtRu) catalyst is equivalent to a 20 nm thick film on a flat substrate surface (thus referred to as the nominal thickness) which is spread along the VACNF sidewall to yield the much smaller particle size and lower local surface density. These are the main catalysts that is employed in this study. Figures 2(d)-2(g) show the STEM-EDS mapping images of VACNF sputtered with Ni film, which confirms the relatively uniform deposition of metal nanoparticles on the entire surface of VACNF.

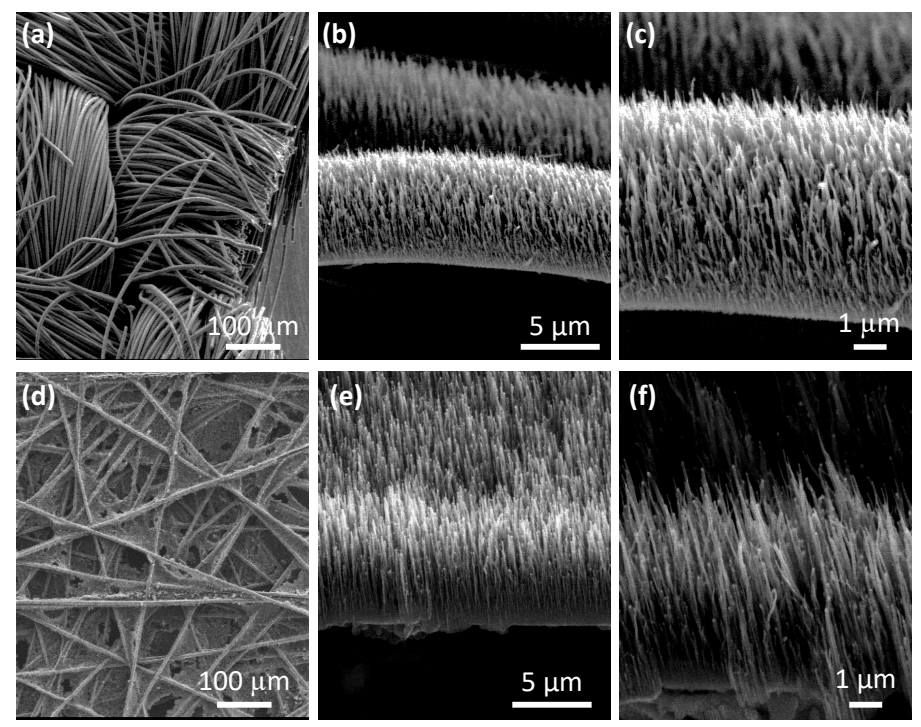


Figure 1 FESEM images of (a) woven structure of CC substrate, (b) and (c) the VACNF array grown on a carbon fiber at the exterior surface of the CC substrate, (d) non-woven structure of CP substrate, and (e) and (f) the VACNF array grown on a carbon fiber at the exterior surface of the CP substrate.

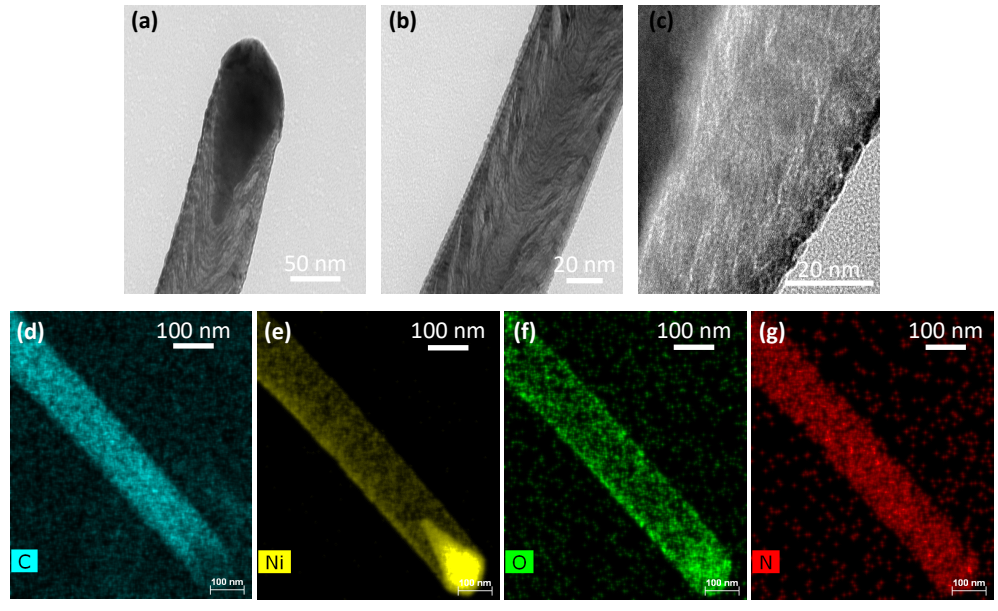


Figure 2 HRTEM images of (a) the tip portion of a VACNF and the much smaller sputtered Ni nanoparticles at the sidewall of the VACNF, (b) and (c) the sidewall of VACNF fiber sputtered with Ni nanoparticles. STEM-EDS mapping images of (d) C, (e) Ni, (f) O, and (g) N deposited on VACNFs.

STEM-EDS mapping images of VACNF-PtRu can be found in our previous publication [46]. From elemental analysis report, the atomic ratio of Pt:Ru is $48.61\%:51.38\% \approx 1:1$ considering the error bars. This is consistent with the composition of the PtRu sputtering target.

The elemental composition of metal nanoparticles deposited on the VACNF surface was analyzed by XPS. Figure 3 shows the high-resolution XPS spectra of C 1s, Ni 2p, Pt 4f, and Ru 3p. The C 1s (Fig. 3(a)) deconvoluted into five distinct peaks at BEs of 284.7, 285.9, 287.8, 291.3, 293.4 eV. These peaks correspond to various states of carbon atoms, including sp²-C, sp³-C, C-O/C-N, C=O, and O-C=O, respectively, with sp²-C hybridized being the

dominating state. Figure 3(b) shows the Ni 2p spectra for VACNF/Ni electrode. The spectra deconvoluted into three pairs of Ni $2p_{3/2}$ and Ni $2p_{1/2}$ doublets. Each doublet is ascribed to Ni(0), Ni(II), and Ni 2p satellite states. Ni(0) correspond to metallic Ni while and Ni(II) are likely from NiO and Ni(OH) $_2$ species. Relative area analysis shows that Ni(II) is the dominating specie, with 77.41% of Ni existing in oxides and hydroxides states, while the metallic Ni(0) constitutes 22.59% of the total deposited Ni. This is not surprising since the sputtered Ni can be easily oxided after exposing to the air.

Figure 3(c) shows the Pt 4f spectra for VACNF-PtRu electrode. The deconvoluted spectra comprised three distinct pairs of Pt $4f_{7/2}$.

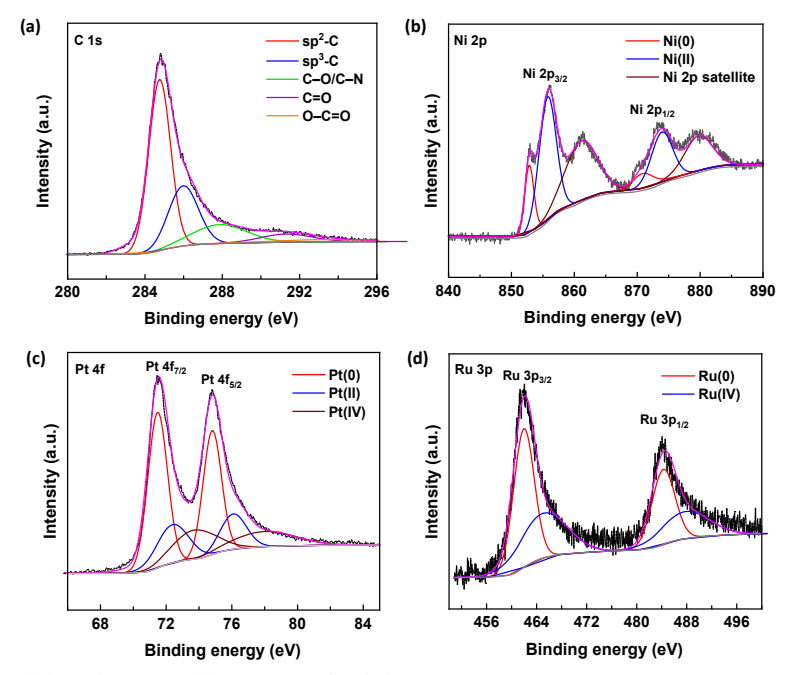


Figure 3 XPS spectra of as-prepared electrodes: (a) C 1s, (b) Ni 2p, (c) Pt 4f, and (d) Ru 3p.

and Pt $4f_{5/2}$ doublets. These three sets of peaks are attributed to Pt(0), Pt(II), and Pt(IV) states. The Pt(0) doublet appearing at 71.5 and 74.8 eV BEs corresponds to metallic Pt, while Pt(II) and Pt(IV) correspond to PtO, Pt(OH)₂ and PtO₂ species, respectively. As per relative area analysis, Pt(0) is the dominating specie, with 55.12% of Pt atoms present in the metallic state. This is followed by Pt(IV) and Pt(II) species, which constitute 22.69% and 22.18% of the total Pt, respectively. For Ru 3p (Fig. 3(d)), two peaks with BEs at 462 and 484.4 eV for Ru $3p_{3/2}$ and Ru $3p_{1/2}$, respectively, correspond to Ru(0) state. The remaining set of peaks are attributed to Ru(IV) state. Metallic Ru i.e., Ru(0) specie, makes up 57.18%, followed by Ru(IV) specie with 42.82% of the Ru in deposited PtRu alloy catalyst.

3.2 Electrochemical performance

3.2.1 Cyclic voltammetry

The electrochemical performance of various LOB cathodes was first evaluated using CV technique incorporated in the LOB assembly. Figure 4 compares the CV curves of LOB employed with Vulcan XC, bare VACNF, VACNF-Ni, and VACNF-PtRu. The cathodic and anodic peaks refer to ORR and OER, respectively. It is evident from the CV curves that VACNF-based cathodes exhibit enhanced ORR activity as compared with Vulcan XC. Furthermore, the incorporation of metal catalysts, i.e., Ni and PtRu, resulted in an even higher current response. Especially, VACNF-Ni outperformed its counterparts by displaying the highest ORR activity though the Ni at the tip of VACNFs that was left from the VACNF growth process may have an additional electrocatalytic contribution. The voltage at which ORR and OER peaks appear is also significant to determine the electrochemical performance of electrodes. Voltages E_1 to E_4 correspond to the formation of Li₂O₂ with various LOB cathodes.

The reduction peaks for VACNF and VACNF-PtRu appeared at a comparable voltage i.e., $E_2 = 2.42$ V and $E_3 = 2.41$ V, respectively. They are followed by Vulcan XC and VACNF-Ni with voltages $E_1 = 2.37$ V and $E_4 = 2.35$ V, respectively. It is noteworthy, at 2.56 V, Vulcan XC displayed a diminished peak

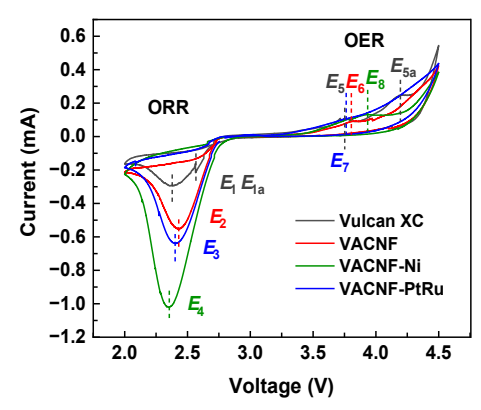


Figure 4 Comparison of CV profiles of LOB incorporated with Vulcan XC, VACNF, VACNF-Ni, and VACNF-PtRu electrodes conducted at the scan rate of 0.1 mV·s⁻¹

 (E_{1a}) which could be attributed to the formation of LiO_2 by the following reaction: $\text{Li}^+ + \text{O}_2 + \text{e}^- \Rightarrow \text{LiO}_2$ [15]. For OER, the oxidation peaks emerge below 4.0 V which correspond to the decomposition of Li_2O_2 by one electron transfer mechanism i.e., $\text{Li}_2\text{O}_2 \Rightarrow \text{Li}^+ + \text{e}^- + \text{LiO}_2$ [15]. Vulcan XC and VACNF-PtRu displayed comparable OER voltage i.e., $E_5 = 3.76$ V and $E_7 = 3.77$ V, respectively. The oxidation peaks for bare VACNF and VACNF/Ni appear at $E_6 = 3.8$ V and $E_8 = 3.92$ V. The anodic peak that appears above 4.0 V refers to the two-electron transfer mechanism, i.e., $\text{Li}_2\text{O}_2 \Rightarrow 2\text{Li}^+ + 2\text{e}^- + \text{O}_2$ [15]. Contrary to VACNF-based electrodes, a pronounced OER peak appeared at 4.19 V with Vulcan XC. This could be attributed to the fact that the majority of the Li_2O_2 disintegration happened above 4.0 V.

3.2.2 Deep discharge tests

Deep discharge tests were conducted to investigate the impact of various cathode electrodes on the electrochemical performance of LOB. Figure 5(a) compares the discharge/charge capacity tests with Vulcan XC, bare VACNF, VACNF-Ni, and VACNF-PtRu coated CC substrate. Each profile represents the maximum areal discharge capacity obtained in the test with the particular

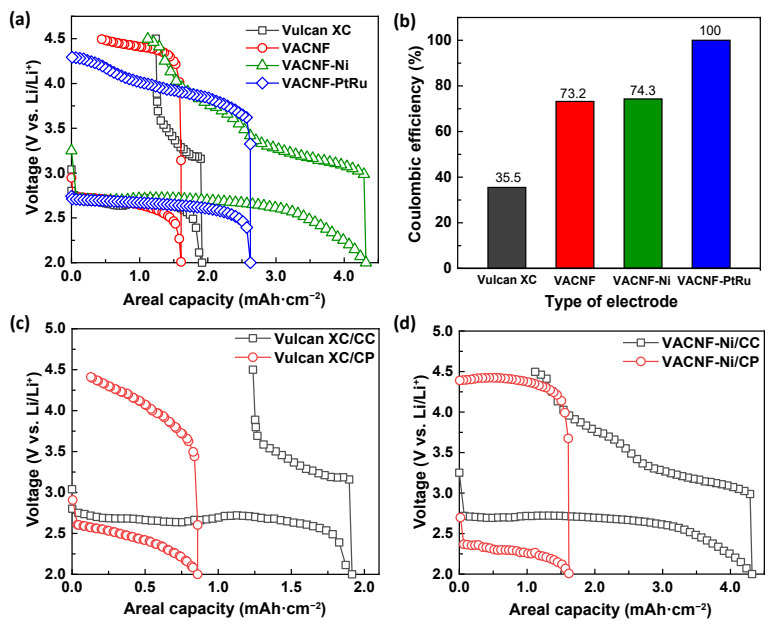


Figure 5 Comparison of (a) maximum areal discharge/charge capacity and (b) Coulombic efficiency of Vulcan XC, bare VACNF, VACNF-Ni, and VACNF-PtRu on CC substrate. Comparison of the performance of CC and CP substrates in terms of maximum areal discharge/charge capacity of (c) Vulcan XC-CC/CP and (d) VACNF-Ni-CC/CP. All tests were conducted at 0.1 mA-cm⁻² current density.

electrode. VACNF-Ni yielded the highest discharge capacity (4.32 mAh·cm⁻²), followed by VACNF-PtRu (2.62 mAh·cm⁻²), Vulcan XC (1.91 mAh·cm⁻²), and bare VACNF (1.60 mAh·cm⁻²). Figure S1 in the ESM compares the specific discharge capacities yielded by the aforementioned cathodes. VACNF-Ni electrode delivered the highest specific discharge capacity (14.92 Ah·g-1) as compared with VACNF-PtRu (9.07 Ah·g⁻¹), bare VACNF (5.55 Ah·g⁻¹), and Vulcan XC (3.83 Ah·g⁻¹). VACNF, generally, are favorable for metal-air batteries as the highly graphitic, freestanding, one-dimensional (1D) structure provides low carbon packing, high void volume, high electronic conductivity, and abundant active reaction sites [21, 23, 35, 36]. High void volume (~ 78%) [35] accommodates the maximum amount of discharge product (Li₂O₂) which results in enhanced discharge capacity. In addition, the binder-free nature helps to reduce unwanted activities, e.g., dissolution in nonaqueous electrolyte, which in turn lowers the adhesion of carbon powders on the substrate [20, 22, 34]. Furthermore, commonly used Teflon and polyvinylidene fluoride (PVDF) binders could involve in side reactions to produce LiF in the discharge cycle [47]. Consequently, the exclusion of polymer binder can improve battery's life span. Moreover, the binder decreases the porosity of the electrode, which eventually affects the mass transfer of oxygen and Li ions and restricts the discharge capacity of the battery. Unlike VACNF, blade-coated Vulcan XC may provide a higher specific surface area, i.e., 260 m²·g⁻¹ [48]. The high surface area could have contributed to its higher areal discharge capacity as compared with bare VANCF. However, the effective utilization of reaction sites could be limited due to the random settlement of carbon powder on the substrate. Contrary to Vulcan XC, the VACNFs are grown homogeneously on substrate fibers without blocking its pores that are essential for mass transfer, whereas blade coated Vulcan XC can cause a decrease in overall porosity.

In addition to VACNF, catalysts Ni and PtRu played a significant role in enhancing battery performance. It is evident from Fig. 4(a) that both catalysts were able to improve discharge capacity by enhancing catalytic activity in comparison with bare VACNF cathode. The catalyst nanoparticles are mostly deposited

in the form of well-deposited nanoparticles (~ 3-5 nm in diameter) on the sidewalls of VACNF in addition to their tips. The catalyst layer introduces roughness on sidewalls and increases surface area [34]. This allows the reaction to occur in the threedimensional (3D) volume across the whole 8 µm tall VACNF array. Moreover, VACNF-Ni yields much lower charge overpotential as compared with its counterparts, a major portion of the charge cycle lies under 3.5 V. Figure 5(b) shows the comparison of Coulombic efficiency (CE) exhibited by each electrode. Due to limited recharging capability, Vulcan XC gave the lowest CE, i.e., 35.5%. LOBs employed with VACNF-based electrodes demonstrated superior CEs. Although VACNF-PtRu displayed relatively lower discharge capacity than VACNF-Ni, nevertheless, it was able to achieve 100% CE. It is noteworthy that the charge potential with VACNF-PtRu did not reach 4.5 V (charge cutoff volatge), unlike other electrodes. This could be attributed to the formation of poorly crystalline Li₂O₂ due to Ru catalytic activity, which disintegrates at comparatively lower voltage during OER [31].

Figures 5(c) and 5(d) show the comparison of discharge/charge capacity tests with different carbon substrates, i.e., CC and CP. First, we compared the discharge capacity performance with Vulcan XC using different substrates. Figure 5(c) shows the comparison of discharge/charge capacity profiles with Vulcan XC/CC and Vulcan XC/CP. The discharge capacity obtained with Vulcan XC/CC is over ~ 2.2 times higher than Vulcan XC/CP. For VACNF-based electrodes, we conducted tests with VACNF-Ni owing to its best performance (Fig. 5(d)). VACNF-Ni/CC achieved 2.65 times higher discharge capacity with much lower overpotential as compared with VACNF-Ni/CP.

Both CC and CP have similar porosity (\sim 0.8) and surface area. But the difference lies in their structure. CC has a woven structure in which carbon fibers are weaved together (Fig. 1(a)). On the contrary, CP has a non-woven structure in which straight carbon fibers are stacked in a multilayer web-like structure and covered with a thin non-continuous carbonaceous film (Fig. 1(d)) [40, 49]. The previous work shows that this difference in their structure forms the basis of the different pore size distributions (PSDs). In

another study by PSD analysis, the mean pore diameter of CC and CP was measured to be 130 μ m [50] and 75 μ m [51], respectively. The mean pore size in CC is almost double that of CP. The bigger pores in CC are between carbon yarns in the weaved pattern [52]. The macropores allow coated material particles to accommodate themselves within the structure as opposed to CP, in which they sit mostly on top. The mass transport property is one of the major challenges in order to ameliorate the performance of Li-O₂ batteries. The transport of Li ions from the electrolyte to reaction sites and incoming oxygen from the other side of the cathode electrode are all related to the mass transport phenomenon. This phenomenon is directly related to pore size and PSD [53, 54]. The possible reason for CC's superior performance is that it offers better mass transport properties. The smaller pores are first clogged during discharging due to the deposition of discharge product. This leads to the blockage of path of incoming oxygen which eventually stops the discharge cycle. On the other hand, the macropores in substrate ensure the transport of oxygen until the battery reaches to its mass transport limitation state. Therefore, the presence of bigger pores in CC allows continuous transport of oxygen for longer period of time. Moreover, CC offers less tortuosity (1.33) [55] as compared with CP ($\tau > 2$) which allows ions to cover less distance before they reach the reaction sites. The tortuosity of VACNF arrays are even smaller, close to 1.

3.2.3 Cycling stability tests

In order to investigate the stability and longevity of VACNF-based electrodes in LOB, cycling stability tests were conducted with a

curtailed areal capacity of 0.5 mAh·cm⁻². Figures 6(a)-6(d) show the cycling stability of Vulcan XC (Fig. 6(a)), VACNF (Fig. 6(b)), VACNF-Ni (Fig. 6(c)), and VACNF-PtRu (Fig. 6(d)). As shown in Fig. 6(e), VACNF-PtRu yielded the highest number of cycles (27 cycles) followed by VACNF-Ni (13 cycles) and bare VACNF (8 cycles). Vulcan XC displayed limited stability by yielding 3 cycles as compared with VACNF-based electrodes. VACNF array provides higher stability due to its graphitic structure. However, bare carbon electrodes could not withstand the corrosive environment of a battery for a longer period of time due to their ability to react with highly electrochemically active intermediate species (superoxide ions) [56]. This leads to the gradual accretion of irreversible discharge product on the cathode surface. Consequently, the battery reaches a point where the reversible discharge product no longer exists during recharging. It is evident from these results that metal catalysts were able to enhance the stability of the cathode electrode. In addition to catalyze ORR and OER, metal nanoparticles covering the sidewalls of VACNF protect the carbon surface from coming into direct contact with intermediate species. This protective layer could be helpful in circumventing the reaction between carbon and unstable superoxide ion, which results in the formation of undesired products, e.g., Li₂CO₃, thereby deteriorating battery life [15]. Moreover, the metal coating allows the reaction to take place at the metal-electrolyte interface instead of the carbon-electrolyte interface. It is interesting to note that despite exhibiting relatively lower discharge capacity in deep discharge tests, PtRu displayed superior cycling stability than Ni. Figure 6(e) compares the

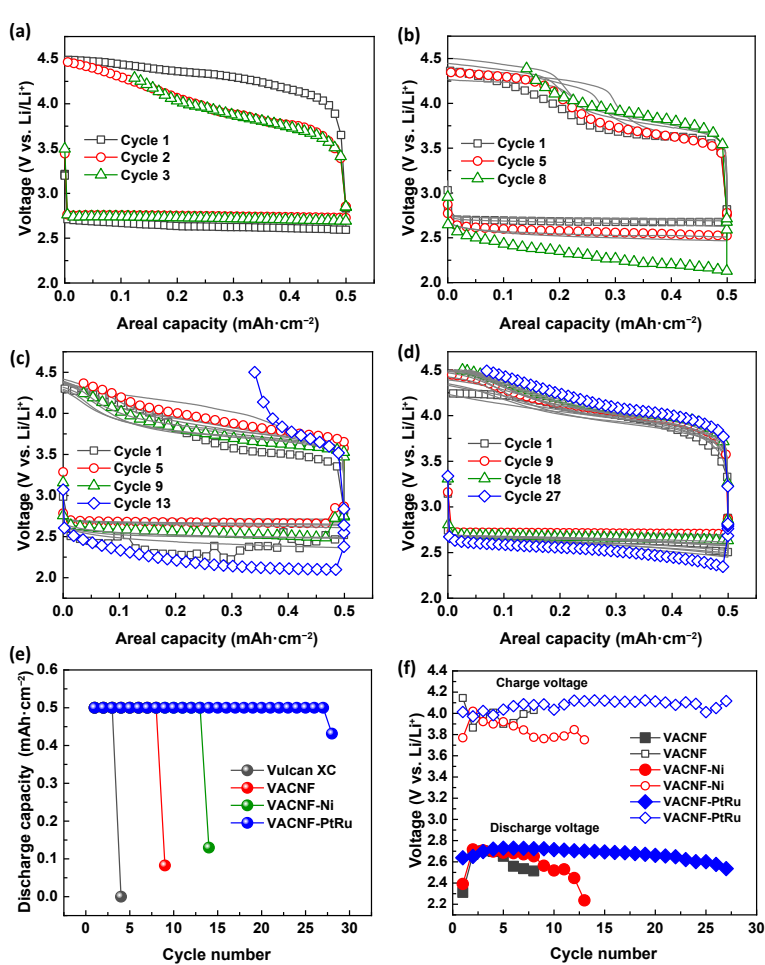


Figure 6 Cycling stability plots of (a) Vulcan XC, (b) VACNF, (c) VACNF-Ni, and (d) VACNF-PtRu on CC substrates with a fixed areal capacity of 0.5 mAh·cm⁻². (e) Discharge capacity vs. cycle number plot and (f) comparison of average discharge and charge voltages yielded by various electrodes in cycling stability tests.

number of cycles achieved with various cathode electrodes. The comparison of average discharge and charge potential of various VACNF-based electrodes are shown in Fig. 6(f). It is noteworthy that VACNF-PtRu yielded higher charge voltage as compared with its counterparts. Nonetheless, it displayed superior performance in stability. This shows that PtRu has suppressed the side reactions by protecting the VACNF from attacking species most effectively compared to other electrodes, leading to a longer battery life. The evolution of cell voltage with number cycles can be ascribed to the instability of electrolyte and evaporation of electrolyte solvent, instability of Li anode, and passivation of cathode surface due to accumulation of irreversible discharge product. It is worth mentioning that VACNF-PtRu exhibited the most stable and consistent capacity-voltage profile in addition to maintaining the highest number of cycles. The sudden voltage drop was not observed with VACNF-PtRu compared to its counterparts. It is evident from Fig. 6(e) that the VACNF-PtRu maintained a high discharge capacity (> 0.4 mAh·cm⁻²) in its 28th cycle as compared to other cathodes (< 0.15 mAh·cm⁻²). This superior performance of PtRu catalyst was also reported in previous studies [30].

It is worth mentioning that various accounts in the literature indicate that achieving high discharge capacity does not always reflect high CE and cycling stability. Yang et al. exploited Pt2Ru/Vulcan XC as a LOB cathode and attained a discharge capacity of 5386 mAh·g⁻¹ compared with Vulcan XC (4376 mAh·g⁻¹) at a current density of 0.05 mA·cm⁻² [32]. A substantial improvement in discharge capacity with the incorporation of Pt2Ru catalyst was not observed. Nevertheless, it maintained a lower charge overpotential than pure carbon electrodes, indicating its catalytic effect on Li₂O₂ oxidation. Similarly, Wu et al. demonstrated higher discharge capacity with Pt/C cathode (> 2000 mAh·g-1) as compared with PtRu/C (< 2000 mAh·g⁻¹) but achieved superior cyclability with the latter (5 vs. 17 cycles). Finally, Zhu and coworkers reached a high discharge capacity of 22,035 mAh·g⁻¹ with Ni/graphene foam cathode but achieved only 22 cycles in cycling stability tests. Herein, we found a trade-off between high discharge capacity, and high CE and cyclability with VACNF-Ni and VACNF-PtRu, respectively. VACNF-PtRu presented the best compromise between decent discharge capacity (9.07 Ah·g⁻¹, 2.62 mAh·cm⁻²) and high CE (100%) and cycling stability (27 cycles).

3.3 Characterization of discharged electrodes

3.3.1 SEM imaging

The morphology of the accumulated discharge product on the cathode surface was examined under FESEM imaging. Figure 7 shows FESEM images of the morphology of deep discharged Vulcan XC (Fig. 7(a)), VACNF-Ni (Figs. 7(b) and 7(d)), and VACNF-PtRu (Fig. 7(c)) cathode electrodes. The discharge product (Li₂O₂) can be seen deposited on the cathode surface. It is evident from the FESEM images that the structure of discharge products in the Vulcan XC cathode is entirely different from VACNF-Ni and VACNF-PtRu. Li₂O₂ exists in the form of big crystalline toroidal structure on Vulcan XC cathode. Each toroid consists of several plate-like structures. On the contrary, VACNF-Ni and VACNF-PtRu yielded spherical and film-like discharge products. The entire surface area of carbon fibers is covered with film-like Li₂O₂. The morphological difference could be explained in terms of the tendency of O2 adsorption/binding with the cathode surface. A cathode with weak O2 binding like Vulcan XC promotes the generation of Li₂O₂ in electrolyte solution via disproportionation ($LiO_2 + LiO_2 \rightarrow Li_2O_2 + O_2$) in the form of big aggregates. The introduction of catalyst onto the cathode surface enhances O2 affinity with the cathode, which leads to the formation of discharge product on the cathode surface via electrochemical reduction (LiO₂ + e^- + Li⁺ \rightarrow Li₂O₂) in the form of film [25]. Interestingly, the alignment of VACNF-Ni is intact after deep discharge, which depicts their higher stability than Vulcan XC (Fig. 7(d)).

3.3.2 XPS analysis

In addition to SEM imaging, the deeply discharged electrodes were analyzed by XPS to evaluate the discharge product with VACNF-based electrodes. Figure 8 shows the Li 1s and O 1s spectra. Regardless of electrode type, BE peaks (54.7 eV) are obtained for Li 1s (Fig. 8(a)), in good agreement with the previous reports for Li₂O₂ [57, 58]. This shows that the majority of the discharge product accumulated is Li₂O₂. For further verification, we deconvoluted O 1s spectra (Fig. 8(b)) of discharged electrodes. A diminished green peak emerged for all electrodes at the BE \sim 532.9 eV, which corresponds to the formation of Li₂CO₃ [59, 60]. It is worth mentioning that the bare VACNF displayed a significantly stronger Li₂CO₃ peak as compared with VACNF-Ni

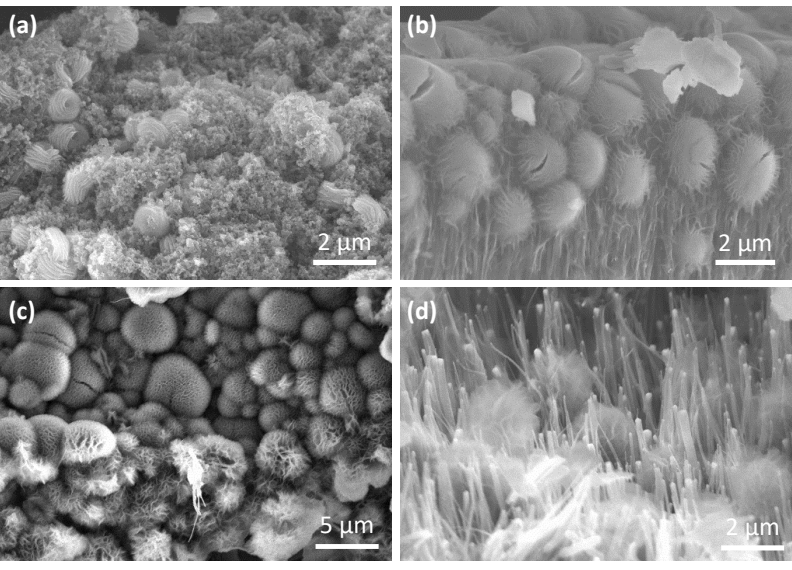


Figure 7 FESEM images of deep discharged (a) Vulcan XC, (b) and (d) VACNF-Ni, and (c) VACNF-PtRu electrodes.

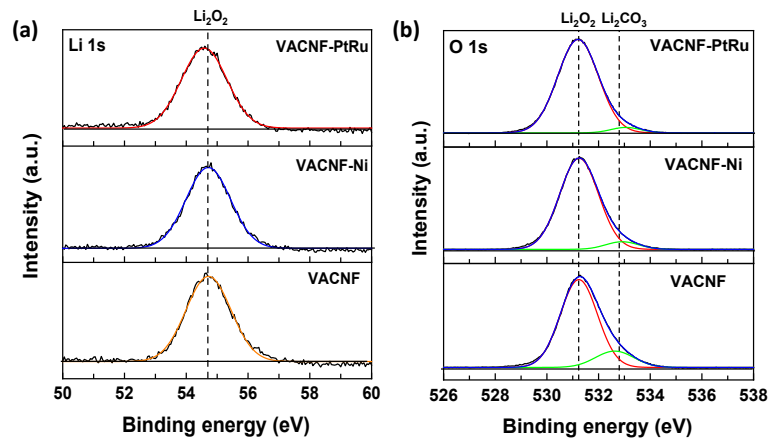


Figure 8 XPS analysis of deep discharged VACNF-based cathode electrodes (a) Li 1s and (b) O 1s.

and VACNF-PtRu. This confirms that the deposited metal catalyst inhibits the generation of unwanted and irreversible discharge products (such as $\rm Li_2CO_3$) by protecting the carbon surface. This leads to the longevity of battery life, as demonstrated by cycling stability results in the previous section.

4 Conclusion

We successfully presented the electrochemical behavior of LOB with the more stable cathode based on graphitic VACNF arrays grown on GDL substrate. Transition metal (Ni) and noble metal alloy (PtRu) deposited on the VACNF array support exhibited significantly improved performance due to their catalytic properties. Deep discharge capacity tests revealed that both catalysts substantially enhanced the discharge capacity as compared with bare VACNF and Vulcan XC. VACNF-Ni achieved the highest specific and areal discharge capacity (14.92 Ah·g⁻¹, 4.32 mAh·cm⁻²). In contrast, VACNF-PtRu cathodes have greatly improved the cycling stability by achieving double the number of cycles as compared to VACNF-Ni. XPS analysis has shown that VACNF-PtRu has proved to be highly effective in suppressing Li₂CO₃ generation. VACNF-PtRu presented the best compromise between decent discharge capacity (9.07 Ah·g-1, 2.62 mAh·cm⁻²) and high CE (100%) and cycling stability (27 cycles). We also investigated the impact of the GDL substrate on LOB performance. Owing to the bimodal PSD, which promotes mass transfer, CC-based electrodes exhibited superior performance in deep discharge tests comparing to CP-based electrodes.

Acknowledgements

S. S. H. Z. and X. L. L. highly appreciate the support from the National Science Foundation (Nos. 1833048 and 1941083). The work by J. L.'s group is partially supported by the National Science Foundation under grant (No. CBET-2054754).

Electronic Supplementary Material: Supplementary material (mass loading of VACNFs and specific capacities of batteries) is available in the online version of this article at https://doi.org/10.26599/NRE.2023.9120055.

Declaration of conflicting interests

The authors declare no conflicting interests regarding the content of this article.

References

- Zaidi, S. S. H.; Li, X. L. Comparing the electrochemical performance of organic and ionic liquid-based electrolytes in lithiumoxygen battery. ECS Meet. Abstr. 2021, MA2021-02, 144.
- [2] Wang, F. Z.; Li, X. L.; Hao, X. W.; Tan, J. Y. Review and recent advances in mass transfer in positive electrodes of aprotic Li-O₂ batteries. ACS Appl. Energy Mater. 2020, 3, 2258–2270.
- [3] Wang, F. Z.; Kahol, P. K.; Gupta, R.; Li, X. L. Experimental studies of carbon electrodes with various surface area for Li-O₂ batteries. *J. Electrochem. Energy Convers. Storage* 2019, 16, 041007.
- [4] Zhou, Y.; Yan, D. F.; Gu, Q. F.; Zhu, S. H.; Wang, L.; Peng, H. G.; Zhao, Y. Implanting cation vacancies in Ni-Fe LDHs for efficient oxygen evolution reactions of lithium-oxygen batteries. *Appl. Catal. B: Environ.* 2021, 285, 119792.
- [5] Zou, X. H.; Lu, Q.; Liao, K. M.; Shao, Z. P. Towards practically accessible aprotic Li-air batteries: Progress and challenges related to oxygen-permeable membranes and cathodes. *Energy Storage Mater*. 2022, 45, 869–902.
- [6] Dong, Y.; Li, S. W.; Hong, S. S.; Wang, L.; Wang, B. Metal-organic frameworks and their derivatives for Li-air batteries. *Chin. Chem. Lett.* 2020, 31, 635–642.
- [7] Balaish, M.; Jung, J. W.; Kim, I. D.; Ein-Eli, Y. A critical review on functionalization of air-cathodes for nonaqueous Li-O₂ Batteries. *Adv. Funct. Mater.* 2020, 30, 1808303.
- [8] Ren, Y. X.; Zhao, T. S.; Tan, P.; Wei, Z. H.; Zhou, X. L. Modeling of an aprotic Li-O₂ battery incorporating multiple-step reactions. *Appl. Energy* 2017, 187, 706–716.
- [9] Bae, Y.; Ko, D. H.; Lee, S.; Lim, H. D.; Kim, Y. J.; Shim, H. S.; Park, H. J.; Ko, Y.; Park, S. K.; Kwon, H. J. et al. Enhanced stability of coated carbon electrode for Li-O₂ batteries and its limitations. *Adv. Energy Mater.* 2018, 8, 1702661.
- [10] Ren, M. Q.; Zhang, J. B.; Zhang, C. H.; Stanford, M. G.; Chyan, Y.; Yao, Y.; Tour, J. M. Quasi-solid-state Li-O₂ batteries with laser-induced graphene cathode catalysts. *ACS Appl. Energy Mater.* 2020, 3, 1702–1709.
- [11] Hegde, G. S.; Ghosh, A.; Badam, R.; Matsumi, N.; Sundara, R. Role of defects in low-cost perovskite catalysts toward ORR and OER in lithium-oxygen batteries. ACS Appl. Energy Mater. 2020, 3, 1338–1348.
- [12] Ding, M. J.; Wang, P.; Zhang, Z. W.; Yin, L. W. Metal-organic framework-derived porous NiCo-layered double hydroxide@MnO₂ hierarchical nanostructures as catalytic cathodes for long-life Li-O₂ batteries. ACS Appl. Energy Mater. 2021, 4, 61–71.
- [13] Zhou, W.; Zhang, H. Z.; Nie, H. J.; Ma, Y. W.; Zhang, Y. N.; Zhang, H. M. Hierarchical micron-sized mesoporous/macroporous graphene with well-tuned surface oxygen chemistry for high capacity and cycling stability Li-O₂ battery. ACS Appl. Mater. Interfaces 2015, 7, 3389–3397.
- [14] Yan, X. N.; Huang, J.; Guo, L. M.; Liu, C. T.; Dong, S. J.; Peng, Z.

- Q. Interrogating lithium-oxygen battery reactions and chemistry with isotope-labeling techniques: A mini review. *Energy Fuels* **2021**, *35*, 4743–4750
- [15] Nam, J. S.; Jung, J. W.; Youn, D. Y.; Cho, S. H.; Cheong, J. Y.; Kim, M. S.; Song, S. W.; Kim, S. J.; Kim, I. D. Free-standing carbon nanofibers protected by a thin metallic iridium layer for extended lifecycle Li-Oxygen batteries. ACS Appl. Mater. Interfaces 2020, 12, 55756–55765.
- [16] Jung, C. Y.; Zhao, T. S.; Zeng, L.; Tan, P. Vertically aligned carbon nanotube-ruthenium dioxide core-shell cathode for non-aqueous lithium-oxygen batteries. J. Power Sources 2016, 331, 82–90.
- [17] Xiao, J.; Wang, D. H.; Xu, W.; Wang, D. Y.; Williford, R. E.; Liu, J.; Zhang, J. G. Optimization of air electrode for Li/Air batteries. *J. Electrochem. Soc.* 2010, 157, A487.
- [18] Zaidi, S. S. H.; Sigdel, S.; Sorensen, C. M.; Kwon, G.; Li, X. L. Incorporation of novel graphene nanosheet materials as cathode catalysts in Li-O₂ battery. *J. Electrochem. Energy Convers. Storage*, in press, DOI: 10.1115/1.4056937.
- [19] Yu, R. M.; Fan, W. G.; Guo, X. X.; Dong, S. M. Highly ordered and ultra-long carbon nanotube arrays as air cathodes for high-energyefficiency Li-oxygen batteries. *J. Power Sources* 2016, 306, 402–407.
- [20] Song, M. J.; Kim, I. T.; Kim, Y. B.; Shin, M. W. Self-standing, binder-free electrospun Co₃O₄/carbon nanofiber composites for nonaqueous Li-air batteries. *Electrochim. Acta* 2015, 182, 289–296.
- [21] Mitchell, R. R.; Gallant, B. M.; Thompson, C. V.; Shao-Horn, Y. All-carbon-nanofiber electrodes for high-energy rechargeable Li-O₂ batteries. *Energy Environ. Sci.* 2011, 4, 2952–2958.
- [22] Song, M. J.; Shin, M. W. Fabrication and characterization of carbon nanofiber@mesoporous carbon core-shell composite for the Li-air battery. *Appl. Surf. Sci.* 2014, 320, 435–440.
- [23] Rahman, M. A.; Wang, X. J.; Wen, C. E. A review of high energy density lithium-air battery technology. J. Appl. Electrochem. 2014, 44, 5-22.
- [24] Ding, Y. J.; Li, Y. J.; Wu, M.; Zhao, H.; Li, Q.; Wu, Z. S. Recent advances and future perspectives of two-dimensional materials for rechargeable Li-O₂ batteries. *Energy Storage Mater.* 2020, 31, 470-491
- [25] Jung, W. B.; Park, H.; Jang, J. S.; Kim, D. Y.; Kim, D. W.; Lim, E.; Kim, J. Y.; Choi, S. Suk, J.; Kang. Y. K. et al. Polyelemental nanoparticles as catalysts for a Li-O₂ battery. ACS Nano 2021, 15, 4235–4244.
- [26] Qin, Y.; Lu, J.; Du, P.; Chen, Z. H.; Ren, Y.; Wu, T. P.; Miller, J. T.; Wen, J. G.; Miller, D. J.; Zhang, Z. C. et al. *In situ* fabrication of porous-carbon-supported α-MnO₂ nanorods at room temperature: Application for rechargeable Li-O₂ batteries. *Energy Environ. Sci.* 2013, 6, 519–531.
- [27] Li, Y. J.; Qin, J. Q.; Ding, Y. J.; Ma, J. X.; Das, P.; Liu, H. Q.; Wu, Z. S.; Bao, X. H. Two-dimensional Mn₃O₄ nanosheets with dominant (101) crystal planes on graphene as efficient oxygen catalysts for ultrahigh capacity and long-life Li-O₂ batteries. ACS Catal. 2022, 12, 12765–12773.
- [28] Shui, J. L.; Du, F.; Xue, C. M.; Li, Q.; Dai, L. M. Vertically aligned N-Doped Coral-like carbon fiber arrays as efficient air electrodes for high-performance nonaqueous Li-O₂ batteries. ACS Nano 2014, 8, 3015–3022.
- [29] Chang, Z. W.; Xu, J. J.; Zhang, X. B. Recent progress in electrocatalyst for Li - O₂ batteries. Adv. Energy Mater. 2017, 7, 1700875.
- [30] Ko, B. K.; Kim, M. K.; Kim, S. H.; Lee, M. A.; Shim, S. E.; Baeck, S. H. Synthesis and electrocatalytic properties of various metals supported on carbon for lithium-air battery. *J. Mol. Catal. A:Chem.* 2013, 379, 9–14.
- [31] Wu, F.; Xing, Y.; Bi, X. X.; Yuan, Y. F.; Wang, H. H.; Shahbazian-Yassar, R.; Li, L.; Chen, R. J.; Lu, J.; Amine, K. Systematic study on the discharge product of Pt-based lithium oxygen batteries. *J. Power Sources* 2016, 332, 96–102.
- [32] Yang, Y.; Liu, W.; Wang, Y. M.; Wang, X. C.; Xiao, L.; Lu, J. T.;

- Zhuang, L. A PtRu catalyzed rechargeable oxygen electrode for Li-O₂ batteries: Performance improvement through Li₂O₂ morphology control. *Phys. Chem. Chem. Phys.* **2014**, *16*, 20618–20623.
- [33] Li, J. X.; Chen, L.; Ye, R. L.; Gao, J. G.; Huang, W. J.; Lin, Y. B.; Huang, Z. G. Improved lithium-O₂ battery performance enabled by catalysts of yolk-shell Fe₃O₄@C mixed with Pt-Ru nanoparticles. *Appl. Surf. Sci.* 2020, 507, 145103.
- [34] Huang, J. Q.; Zhang, B.; Xie, Y. Y.; Lye, W. W. K.; Xu, Z. L.; Abouali, S.; Akbari Garakani, M.; Huang, J. Q.; Zhang, T. Y.; Huang, B. L. et al. Electrospun graphitic carbon nanofibers with *in-situ* encapsulated Co-Ni nanoparticles as freestanding electrodes for Li-O₂ batteries. *Carbon* 2016, 100, 329–336.
- [35] Chen, Y. Z.; Elangovan, A.; Zeng, D. L.; Zhang, Y. F.; Ke, H. Z.; Li, J.; Sun, Y. B.; Cheng, H. S. Vertically aligned carbon nanofibers on Cu foil as a 3D current collector for reversible Li Plating/Stripping toward High-Performance Li-S Batteries. *Adv. Funct. Mater.* 2020, 30, 1906444.
- [36] Li, J.; Pandey, G. P. Advanced physical chemistry of carbon nanotubes. *Annu. Rev. Phys. Chem.* 2015, 66, 331–356.
- [37] Shu, C. Z.; Liu, Y. H.; Long, J. P.; Chen, X. F.; Su, Y. 3D array of Bi₂S₃ nanorods supported on Ni foam as a highly efficient integrated oxygen electrode for the lithium-oxygen battery. *Part. Syst. Charact.* 2018, 35, 1700433.
- [38] Li, J. X.; Zhao, Y.; Zou, M. Z.; Wu, C. X.; Huang, Z. G.; Guan, L. H. An effective integrated design for enhanced cathodes of Ni foam-supported Pt/carbon nanotubes for Li-O₂ batteries. ACS Appl. Mater. Interfaces 2014, 6, 12479–12485.
- [39] Zhu, T. J.; Li, X. Y.; Zhang, Y.; Yuan, M. W.; Sun, Z. M.; Ma, S. L.; Li, H. F.; Sun, G. B. Three-dimensional reticular material NiO/Nigraphene foam as cathode catalyst for high capacity lithium-oxygen battery. *J. Electroanal. Chem.* 2018, 823, 73–79.
- [40] Radhakrishnan, V.; Haridoss, P. Differences in structure and property of carbon paper and carbon cloth diffusion media and their impact on proton exchange membrane fuel cell flow field design. *Mater. Des.* 2011, 32, 861–868.
- [41] Jiang, H. R.; Zeng, Y. K.; Wu, M. C.; Shyy, W.; Zhao, T. S. A uniformly distributed bismuth nanoparticle-modified carbon cloth electrode for vanadium redox flow batteries. *Appl. Energy* 2019, 240, 226–235.
- [42] Forner-Cuenca, A.; Penn, E. E.; Oliveira, A. M.; Brushett, F. R. Exploring the role of electrode microstructure on the performance of non-aqueous redox flow batteries. *J. Electrochem. Soc.* 2019, 166, A2230–A2241.
- [43] Wang, F. Z.; Li, X. L. Effects of the electrode wettability on the deep discharge capacity of Li-O₂ batteries. ACS Omega 2018, 3, 6006–6012.
- [44] Mohazabrad, F.; Wang, F. Z.; Li, X. L. In fluence of the oxygen electrode open ratio and electrolyte evaporation on the performance of Li-O₂ batteries. ACS Appl. Mater. Interfaces 2017, 9, 15459–15469.
- [45] Elangovan, A.; Xu, J. Y.; Brown, E.; Liu, B.; Li, J. Fundamental electrochemical insights of vertically aligned carbon nanofiber architecture as a catalyst support for ORR. *J. Electrochem. Soc.* 2020, 167, 066523.
- [46] Elangovan, A.; Xu, J. Y.; Sekar, A.; Liu, B.; Li, J. Enhancing methanol oxidation reaction with platinum-based catalysts using a Ndoped three-dimensional graphitic carbon support. *ChemCatChem* 2020, 12, 6000–6012.
- [47] Xu, W.; Hu, J. Z.; Engelhard, M. H.; Towne, S. A.; Hardy, J. S.; Xiao, J.; Feng, J.; Hu, M. Y.; Zhang, J.; Ding, F. et al. The stability of organic solvents and carbon electrode in nonaqueous Li-O₂ batteries. *J. Power Sources* 2012, 215, 240–247.
- [48] Holade, Y.; Morais, C.; Servat, K.; Napporn, T. W.; Kokoh, K. B. Enhancing the available specific surface area of carbon supports to boost the electroactivity of nanostructured Pt catalysts. *Phys. Chem. Chem. Phys.* 2014, 16, 25609–25620.

- [49] El-Kharouf, A.; Mason, T. J.; Brett, D. J. L.; Pollet, B. G. Ex-situ characterisation of gas diffusion layers for proton exchange membrane fuel cells. J. Power Sources 2012, 218, 393–404.
- [50] Allioux, F. M.; Kapruwan, P.; Milne, N.; Kong, L. X.; Fattaccioli, J.; Chen, Y.; Dumée, L. F. Electro-capture of heavy metal ions with carbon cloth integrated microfluidic devices. *Sep. Purif. Technol.* 2018, 194, 26–32.
- [51] Ribadeneyra, M. C.; Grogan, L.; Au, H.; Schlee, P.; Herou, S.; Neville, T.; Cullen, P. L.; Kok, M. D. R.; Hosseinaei, O.; Danielsson, S. et al. Lignin-derived electrospun freestanding carbons as alternative electrodes for redox flow batteries. *Carbon* 2020, 157, 847–856.
- [52] Park, S.; Popov, B. N. Effect of a GDL based on carbon paper or carbon cloth on PEM fuel cell performance. *Fuel* 2011, 90, 436–440.
- [53] Zaidi, S. S. H.; Li, X. L. Effects of oxygen cathode substrates with various carbon catalysts on the discharge capacity of lithium-oxygen battery.. ECS Meet. Abstr. 2021, MA2021-01, 350.
- [54] Zhou, X. L.; Zhao, T. S.; Zeng, Y. K.; An, L.; Wei, L. A highly permeable and enhanced surface area carbon-cloth electrode for vanadium redox flow batteries. J. Power Sources 2016, 329, 247–254.
- [55] Tenny, K. M.; Forner-Cuenca, A.; Chiang, Y. M.; Brushett, F. R.

- Comparing physical and electrochemical properties of different weave patterns for carbon cloth electrodes in redox flow batteries. *J. Electrochem. Energy Convers. Storage* **2020**, *17*, 041010.
- [56] Ottakam Thotiyl, M. M.; Freunberger, S. A.; Peng, Z. Q.; Bruce, P. G. The carbon electrode in nonaqueous Li-O₂ cells. *J. Am. Chem. Soc.* 2013, 135, 494–500.
- [57] Schroeder, M. A.; Pearse, A. J.; Kozen, A. C.; Chen, X. Y.; Gregorczyk, K.; Han, X. G.; Cao, A. Y.; Hu, L. B.; Lee, S. B.; Rubloff, G. W. et al. Investigation of the cathode-catalyst-electrolyte interface in aprotic Li-O₂ batteries. *Chem. Mater.* 2015, 27, 5305–5313.
- [58] Wood, K. N.; Teeter, G. XPS on Li-battery-related compounds: Analysis of inorganic SEI phases and a methodology for charge correction. ACS Appl. Energy Mater. 2018, 1, 4493–4504.
- [59] Wong, R. A.; Dutta, A.; Yang, C. Z.; Yamanaka, K.; Ohta, T.; Nakao, A.; Waki, K.; Byon, H. R. Structurally tuning Li₂O₂ by controlling the surface properties of carbon electrodes: Implications for Li-O₂ batteries. *Chem. Mater.* 2016, 28, 8006–8015.
- [60] Yue, K.; Zhai, C. X.; Gu, S. N.; Yeo, J.; Zhou, G. W. The effect of ionic liquid-based electrolytes for dendrite-inhibited and performance-boosted lithium metal batteries. *Electrochim. Acta* 2022, 401, 139527.

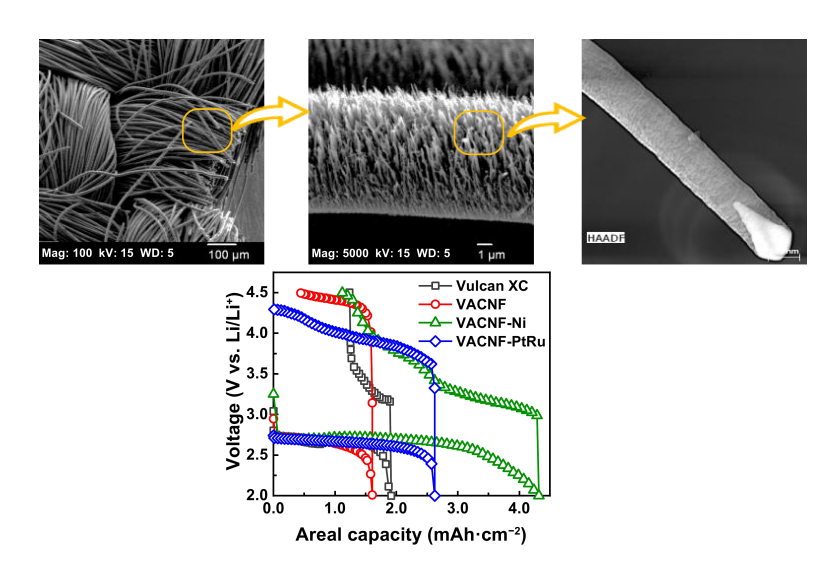


Syed Shoaib Hassan Zaidi has received master's degree from University of Texas at Arlington. Currently, he is pursuing PhD. in Mechanical Engineering at University of Kansas. His research is focused on next generation energy storage devices such as Li-O₂ Batteries.



Xianglin Li is an Associate Professor at the Department of Mechanical Engineering and Materials Science at Washington University in St. Louis (WashU). His current research projects are closely related to energy technologies, including direct methanol fuel cells, Li-O₂ batteries, battery thermal management, and advanced heat transfer systems.

Table of contents



 Li-O_2 battery cathode based on vertically aligned carbon nanofibers sputtered with noble metal alloy (PtRu) and transition metal (Ni) electrocatalysts demonstrated enhanced electrochemical performance.

Electronic Supplementary Material

Binder-free Li-O₂ battery cathodes using Ni- and PtRu-coated vertically aligned carbon nanofibers as electrocatalysts for enhanced stability

Syed Shoaib Hassan Zaidi¹, Sabari Rajendran², Archana Sekar², Ayyappan Elangovan², Jun Li², and Xianglin Li ^{1,3} ()

Supporting information to https://doi.org/10.26599/NRE.2023.9120055

¹ Department of Mechanical Engineering, University of Kansas, Lawrence, KS 66045, USA

² Department of Chemistry, Kansas State University, Manhattan, KS 66506, USA

³ Department of Mechanical Engineering and Materials Science, Washington University in St. Louis, St. Louis, MO 63130, USA

1. Experimentally determined mass loadings of VACNF samples:

The details of the experimentally measured VACNF mass loadings are shown in Table S1. For all the samples, the mass of the substrate was measured before and after the VACNF growth process. It is to be noted that there is a difference in the area of the bare substrate and the area of grown VACNF. From the measured values, the areal mass loading was calculated. In general, the experimentally determined mass loadings are lower compared to the theoretically estimated loading (0.32 mgcm⁻²). Also, there is a significant difference in the mass loading between carbon paper and carbon cloth substrates. It is noteworthy that the experimentally determined VACNF mass loading by this method may not reflect the true values since there could be mass losses associated with the carbon substrate during the growth process.

Table S1. Summary of mass loading calculations of VACNF-based electrodes.

Sample	Sample area (cm²)	Initial mass (mg)	Final mass (mg)		VACNF areal mass loading (mg cm ⁻²)
VACNF/CC	4.91	76.2 ± 0.1	77.6 ± 0.1	1.4 ± 0.1	0.285
Ni/VACNF/CC	4.85	75.5 ± 0.1	76.9 ± 0.1	1.4 ± 0.1	0.288
PtRu/VACNF/CC	4.70	73.6 ± 0.1	75 ± 0.1	1.4 ± 0.1	0.298
Ni/VACNF/CP	4.96	19.6 ± 0.1	20.3 ± 0.1	0.7 ± 0.1	0.141

2. Comparison of Specific Capacity plot:

Fig. S1 compares the maximum specific discharge/charge capacity yielded by VACNF-based electrodes and Vulcan XC. VACNF-Ni electrode displayed the highest specific discharge capacity

of 14.92 Ah g^{-1} followed by VACNF-PtRu (9.07 Ah g^{-1}), bare VACNF (5.55 Ah g^{-1}) and Vulcan XC (3.83 Ah g^{-1}).

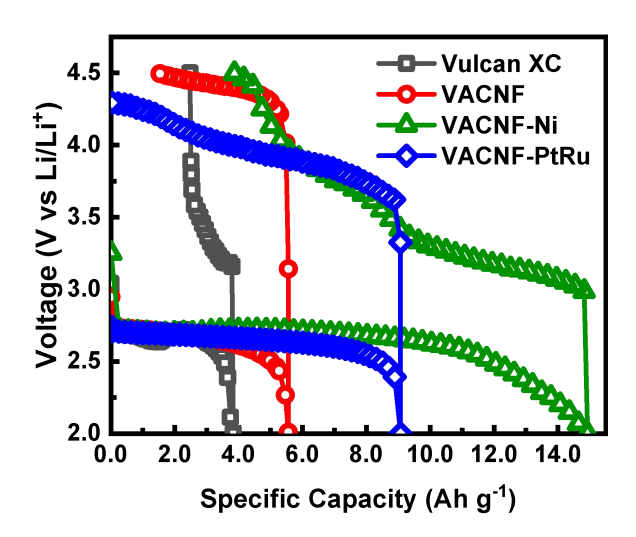


Figure S1 Comparison of maximum specific discharge/charge capacity of LOB employed with Vulcan XC, Bare VACNF, VACNF-Ni, and VACNF-PtRu as cathode. All tests were conducted at 0.1 mA cm⁻² current density.